crystals

Article

Tuning Fe_2Ti Distribution to Enhance Extrinsic Magnetic Properties of $SmFe_{12}$-Based Magnets

Jinbo Wei [1], Shuainan Xu [1], Chengyuan Xu [1], Xiaolian Liu [1], Yu Pan [1,*], Wei Wang [2], Yue Wu [2], Ping Chen [2], Jun Liu [2], Lizhong Zhao [1] and Xuefeng Zhang [1,*]

1 Institute of Advanced Magnetic Materials, College of Materials and Environmental Engineering, Hangzhou Dianzi University, Hangzhou 310012, China; 211200001@hdu.edu.cn (J.W.); xushuainan.123@163.com (S.X.); 211200029@hdu.edu.cn (C.X.); liuxiaolian@hdu.edu.cn (X.L.); lzzhao@hdu.edu.cn (L.Z.)

2 Ningbo Shouzheng Magnet Co., Ltd., Ningbo 315000, China; wangwei_017@163.com (W.W.); mamm@szemagnet.com (Y.W.); chenp@szemagnet.com (P.C.); fallway@126.com (J.L.)

* Correspondence: yupan@hdu.edu.cn (Y.P.); zhang@hdu.edu.cn (X.Z.)

Abstract: The $ThMn_{12}$-type $SmFe_{12}$-based rare-earth permanent magnet has attracted widespread attention due to its excellent intrinsic magnetic properties and high-temperature stability. However, the challenge in realizing continuous non-magnetic or weakly magnetic grain boundary phases equilibrated with the $SmFe_{12}$ main phase hinders the enhancement in extrinsic magnetic properties of the $SmFe_{12}$-based permanent magnet, especially for the coercivity. In this work, by controlling the cooling rate, the uniform distribution of paramagnetic Fe_2Ti phases at grain boundaries is achieved in the $SmFe_{12}$-based alloy ribbon, resulting in a high coercivity of 7.95 kOe. This improvement is attributed to the elimination of the impurity phase within the $SmFe_{12}$ main phase and the magnetic isolation effect of the grain boundary phase composed of paramagnetic Fe_2Ti, which is directly observed by transmission electron microscopy and further confirmed by micromagnetic simulation. Moreover, first-principles calculations show that the V element can dope into Fe_2Ti and facilitate the transition of its paramagnetic state at room temperature. This study provides new insights into constructing weakly magnetic grain boundary phases for $SmFe_{12}$-based permanent magnets, offering a novel approach to enhance coercivity.

Keywords: $SmFe_{12}$-based magnet; paramagnetic Fe_2Ti; grain boundary phases; coercivity

check for updates

Citation: Wei, J.; Xu, S.; Xu, C.; Liu, X.; Pan, Y.; Wang, W.; Wu, Y.; Chen, P.; Liu, J.; Zhao, L.; et al. Tuning Fe_2Ti Distribution to Enhance Extrinsic Magnetic Properties of $SmFe_{12}$-Based Magnets. *Crystals* **2024**, *14*, 572. https://doi.org/10.3390/cryst14060572

Academic Editor: Jan Macutkevic

Received: 20 May 2024
Revised: 8 June 2024
Accepted: 16 June 2024
Published: 20 June 2024

1. Introduction

Due to the development of clean and green energy technology, emerging industries such as wind power generation and new energy motors require rare-earth permanent magnet materials superior to NdFeB [1–4]. The $ThMn_{12}$-type $SmFe_{12}$-based permanent magnet is acknowledged as a promising candidate due to its superior intrinsic magnetic properties and inherent high-temperature stability [5,6]. However, due to the inability to construct ideal non-magnetic or weakly magnetic grain boundary phases, there are challenges in effectively converting its outstanding intrinsic properties into extrinsic performance, mainly its coercivity.

For $ThMn_{12}$-type alloys, achieving high coercivity that is similar to Nd-Fe-B relies on constructing uniformly continuous non-magnetic grain boundary phases to isolate its intergranular magnetic interactions [7]. Unlike NdFeB, the metastability of $SmFe_{12}$ makes it difficult to form Sm-rich grain boundary phases. Studies have confirmed that introducing V as a stabilizing element in the $SmFe_{12}$-based compound is essential to forming Sm-rich grain boundary phases [8–10], which is advantageous for the magnetic isolation effect. However, the presence of higher iron content in the rich Sm grain boundary phase and ferromagnetic phases like $SmFe_2$ and $SmFe_3$ weakens its magnetic isolation effect [11,12]. Recent research has demonstrated the feasibility of constructing continuous non-magnetic grain boundary phases in bulk $SmFe_{12}$-based magnets [9,13,14]. A magnet with a composition of SmFeTiVGaAl exhibited relatively continuous weak magnetic grain boundary phases and a paramagnetic phase Fe_2Ti [15], so the addition of Ga and al elements is conducive to the formation of grain boundary phases [9]. Liu et al. introduced Ti-rich Fe_2Ti grain boundary phases in $Sm(Fe_{0.8}Co_{0.2})_{11}TiB_X$ alloys, which enhanced magnetic isolation between grains, resulting in an increase in coercivity from 3 kOe to 6 kOe and remanence from 61 emu/g to 75 emu/g; however [16], the introduction of Fe_2Ti leads to the depletion of the rich Sm phase at the grain boundaries, which can affect the stability of the $SmFe_{12}$ phase during subsequent bulk magnet processing [17]. Currently, there are challenges in controlling the distribution of Fe_2Ti to the grain boundaries without disrupting the Sm-rich grain boundary phase.

In this study, we tune the speeds of melt spinning to control the cooling rate of the $Sm_8Fe_{73.5}Ti_8V_8Al_2Ga_{0.5}$ alloy, realizing the distribution of Laves phase Fe_2Ti within the grain boundary phase combined with the Sm-rich phase, thereby achieving a high coercivity of 7.95 kOe of $SmFe_{12}$-based alloy ribbon at a cooling rate of 13 m/s. Transmission electron microscopy (TEM) characterization shows that optimal cooling rates can eliminate the Fe_2Ti phase within the main phase, tune its distribution into grain boundaries, and enable it to combine with Sm-rich phases, enhancing its magnetic isolation effect. The micromagnetic simulation demonstrates the beneficial synergistic effect of Laves phase Fe_2Ti with Sm-rich phases in enhancing the coercivity of the $SmFe_{12}$-based alloy. Furthermore, first-principles calculations reveal that doping V elements into Fe_2Ti facilitates its paramagnetic formation at room temperature, thereby enhancing its magnetic isolation effect. Our research provides a novel approach for achieving magnetic isolation by weakly magnetic Fe_2Ti grain boundary phases and developing high-coercivity $SmFe_{12}$-based magnets.

2. Materials and Methods

To obtain an alloy with a uniform composition and a complete structure, the nominal composition of $Sm_8Fe_{73.5}Ti_8V_8Al_2Ga_{0.5}$ ingot was prepared using the strip-casting process [13]. The elements Sm, Fe, Ti, V, Al, and Ga, each with a purity of 99.9%, were mixed and melted before being cast onto a copper rod with a surface speed of 1.5 m/s to form alloy strips. An excess of 50% Sm was added to compensate due to the volatility of Sm. Subsequently, the strips were compressed into small blocks weighing 5~8 g each and placed into quartz tubes with apertures ranging from 0.5 to 0.6 mm. The size of quartz tube opening was fixed at approximately 0.7 mm above the copper roller. Melt spinning ribbons with the wheel speeds of 4 m/s, 8 m/s, 13 m/s, 18 m/s, 23 m/s, and 33 m/s were then prepared in sequence. The thickness of the ribbons ranged from 20 to 60 μm. In this study, the wheel speed is positively correlated with the cooling rate of the alloy.

The density of the samples was measured using the Archimedean method. The magnetic properties of the samples at room temperature were measured by using a magnetic measurement system equipped with a 7 T vibrating sample magnetometer (MPMS Quantum Design, Pfungstadt, Germany). The sample mass ranged from 5 to 10 mg. The demagnetization coefficient (f) for the ribbons was set to 0, as the measurement direction was parallel to the surface plane of the ribbons. X-ray diffraction (XRD, Rigaku Smartlab with Cu-Ka radiation, Tokyo, Japan) determined the ribbons' crystal structure and phase components. The Rietveld refinement of XRD, including phase constitution and lattice parameters, was carried out using the GSAS-II software (Version 5304) [18]. The microstructure was characterized by transmission electron microscope, and the magnetic domain structure was observed using a Lorentz TEM (Talos F200S, FEICo., Bangkok, Thailand) in Fresnel mode. The data obtained using the instruments and testing methods described above are sufficient to support the results of this study. Due to limitations in our conditions, we did not employ the more precise Mössbauer spectroscopy [19,20] to measure the material's purity and magnetic properties.

To explore the effect of the distribution of the Fe_2Ti phase on the μ_0H_c, a finite element micromagnetic package carried out the micromagnetic simulations with magpar [21]. The material parameters of the 1:12 grain model were set as follows: saturation magnetization M_s = 0.97 T, magnetocrystalline anisotropy constant K_1 = 3.7 MJ/m^3, and exchange stiffness A = 7.2 pJ/m. The GB phase was defined as an amorphous phase with parameters of M_s = 0.45 T, K_1 = 0 MJ/m^3, and A = 1.55 pJ/m [14]. The parameters of the Fe_2Ti phase were set as M_s = 0 T, K_1 = 0 MJ/m^3, and A = 0 pJ/m due to its paramagnetic nature at room temperature.

The DFT calculations were carried out by utilizing the OpenMX open-source package (Ver. 3.8), with norm-conserving pseudopotentials and pseudoatomic–orbital basis sets [22–25]. The Perdew–Burke–Ernzerhof (PBE) functional within the generalized gradient approximation (GGA) was employed to characterize the exchange correlation interactions of electrons [26,27]. An 8 × 8 × 4 K-point mesh coupled with a truncation energy of 400 Ry was selected after the truncation energy test. Convergence criteria for structural optimization and self-consistent calculations were 5×10^{-4} Hartree/Bohr. and 10^{-6} Hartree, respectively. The selection of the local basis set was as follows: Ti7.0-s3p3d3f1, Ti_PBE19, Fe6.0S-s2p2d1, Fe_PBE19S, V6.0-s2p2d2, V_PBE19. The stability of the lattice structure was evaluated by calculating the formation energy of the compound. The forming energy ΔE is defined as follows:

$$\Delta E[Fe_2Ti_{0.75}V_{0.25}] \equiv E[Fe_2Ti_{0.75}V_{0.25}] - 2E[Fe] - 0.75E[Ti] - 0.25E[V] \quad (1)$$

In Formula (1), $E[Fe_2TiV]$ represents the total energy after optimizing the standard crystal cell structure, while $E[Fe]$, $E[Ti]$, and $E[V]$ represent the energies of Fe, Ti, and V bulk, respectively.

For magnetic properties calculation, a denser K-point mesh of 14 × 14 × 10 was used. The selected local basis set was as follows: Ti7.0-s3p3d3f1, Ti_PBE19, Fe6.0H-s3p2d2f1, Fe_PBE19H, V6.0-s2p2d2, V_PBE19. The magnetic anisotropy energy (MAE) of an Fe_2Ti was evaluated in a self-consistent manner based on the total energy.

$$K_u = E_a - E_c \quad (2)$$

In Formula (2), E_a and E_c are the total energy as magnetization along the *a* and *c* axes, respectively. The positive and negative of K_u represent uniaxial anisotropy and planar anisotropy, respectively. The total magnetic moment includes the spin magnetic moment and the orbital magnetic moment. Since the orbital magnetic moment is in the form of spin–orbit coupling (SOC), the orbital magnetic moment is calculated under non-collinear DFT calculations. The magnetic exchange couplings between Fe atoms were calculated by OpenMX based on Green's functional representation of the Liechtenstein formula [28–30].

3. Results and Discussion

3.1. XRD Analysis and Magnetic Properties

To investigate the phase composition and magnetic properties of the alloys at different cooling rates, XRD and magnetic properties were tested. Figure 1a,b present the XRD refined data and phase composition ratio graphs of rapidly solidified alloys with different cooling rates. It reveals that the 1.5 m/s strip alloy is composed of 1:12, Laves Fe_2Ti, and has a low content of α-Fe phases. All the 1:12 main phase content ratios were consistently above 90 wt%, increasing with the rising cooling rate, whereas the content of Fe_2Ti first increases with the cooling rates, reaches a max of 9.4% at 13 m/s, and then decreases. Furthermore, the soft magnetic α-Fe phase is only observed in the 1.5 m/s, 4 m/s, and 8 m/s alloys. As the cooling rate increases to 13 m/s and beyond, the XRD refined data indicate the disappearance of the α-Fe phase and a decrease in Laves phase Fe_2Ti. The content of the 1:12 phase gradually increases, reaching its highest in the 33 m/s sample, due to the decreasing crystallinity and increasing amount of amorphous material with the increase in the strip-casting rate [31,32]. XRD data show an increase in the peak width of the 1:12 phase, and the total content of Fe_2Ti and α-Fe gradually decreases [33].

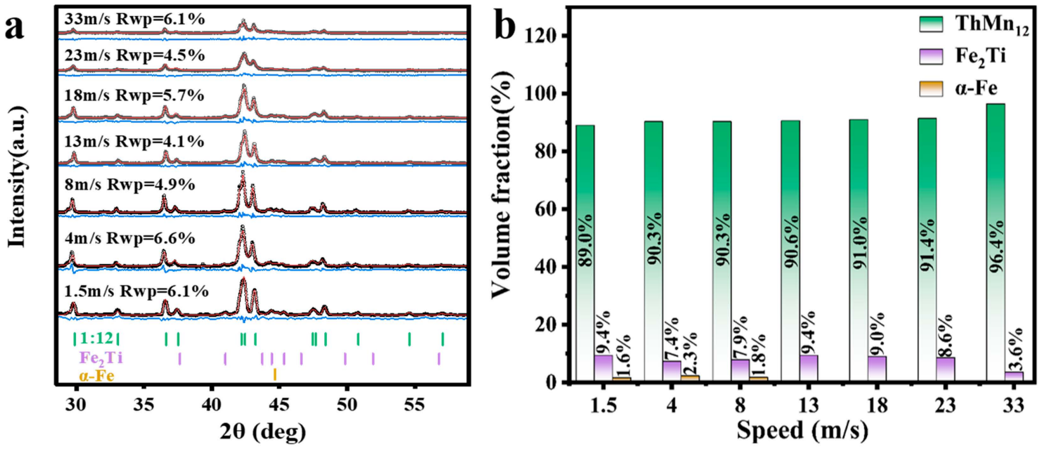

Figure 1. Refined XRD patterns (**a**) and the phase constitution (**b**) of the $Sm_8Fe_{73.5}Ti_8V_8Al_2Ga_{0.5}$ alloys with different cooling rates varying from 1.5 m/s to 33 m/s.

Figure 2a presents the demagnetization curves of the alloy with different speeds, while Figure 2b reveals the variation curves of coercivity and remanence among the samples with different cooling rates. More information on the demagnetization curves in the second quadrant is provided in Figure S1. A smaller range of cooling rates of the samples with magnetic properties are shown in Table S1 and Figure S2 to assess the variability in coercivity. The coercivities and remanences of these samples show an initial rise followed by a drop with the increasing cooling rates. The optimal magnetic performance is observed in samples with cooling rates at 13 m/s and 18 m/s, with coercivities of 7.95 kOe and 7.94 kOe and remanences of 3.59 kGs and 3.57 kGs, respectively. At 13 m/s, the absence of α-Fe and the maximized Fe_2Ti content resulted in the sample exhibiting the highest coercivity. Therefore, the paramagnetic phase Fe_2Ti contributes to the enhancement in coercivity [12]. Samples with cooling rates exceeding 18 m/s exhibit a rapid decrease in both coercivity and remanence. The main reason is that at high cooling rates, it is difficult for the sample to form the hard magnetic main phase $SmFe_{12}$ [34].

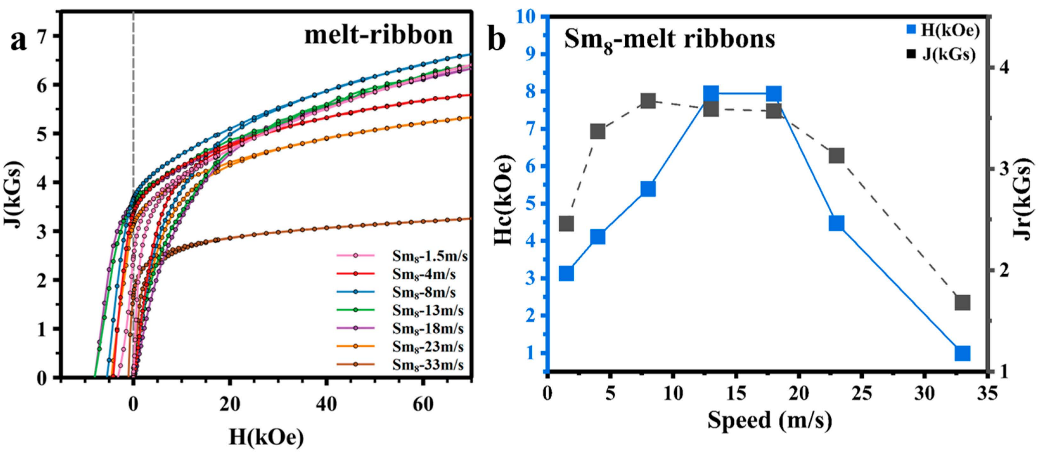

Figure 2. Demagnetization curve (**a**) and magnetic properties change curve of the $Sm_8Fe_{73.5}Ti_8V_8Al_2Ga_{0.5}$ alloys (**b**) with different cooling rates varying from 1.5 m/s to 33 m/s.

3.2. Microstructure

To investigate the microstructure and elemental distributions of the alloys, we select four samples with cooling rates of 1.5 m/s, 4 m/s, 13 m/s, and 23 m/s, characterized under the high-angle annular dark-field (HAADF) mode and energy-dispersive spectroscopy (EDS) of TEM, as shown in Figure 3a–d. In the 1.5 m/s sample, the grain size of the 1:12 main phase is in the micron range, while it is in the nanometer scale in the other samples. In the Ti-Ga-Sm elemental mapping, large Ti-based particles are observed at triple junctions, while small Ti-based particles appear inside the 1:12 main phase, which represents the existence of Fe_2Ti grains. As the cooling rate increases to 4 m/s, Fe_2Ti inside the 1:12 main phase gradually disappears. Sm, Ga, and Al elements of the grain boundary phase are mostly distributed at triple junctions, while the distribution of Fe and V elements is mainly inside the 1:12 main phase and Fe_2Ti grain, with almost no presence at grain boundaries. Detailed characterization of 4 m/s samples can be seen in Figure S3. When the cooling rate increases to 13 m/s, the rich Sm, Ga, and Al phases in the alloy gradually form a continuous grain boundary phase along with Fe_2Ti, the Fe_2Ti phase inside the 1:12 main phase completely disappears. However, as the cooling rate increases to 23 m/s, the continuity of the grain boundary phase is disrupted. It shows that the Sm, Al, and Ga elements are enriched at the grain boundary, leading to significant grain boundary segregation, while the Fe_2Ti phase is randomly distributed. The microstructure characterization of the 23 m/s sample can be seen in Figure S4. It demonstrates that the Fe_2Ti grains in the main phase can be eliminated and distributed in the grain boundary at the optimal cooling rate. This phenomenon is due to the non-uniform nucleation of Fe_2Ti, which will first nucleate at the grain boundary and then nucleate within the grain [35]. At a specific cooling rate, the alloy gradually forms a continuous grain boundary phase containing Fe_2Ti, and Fe_2Ti disappears in the 1:12 phase, which is beneficial to increases in the coercivity of the alloy. An EDS picture of a single element in samples with different cooling rates is shown in Figure S5. These EDS images of single elements can better determine the composition of different phases.

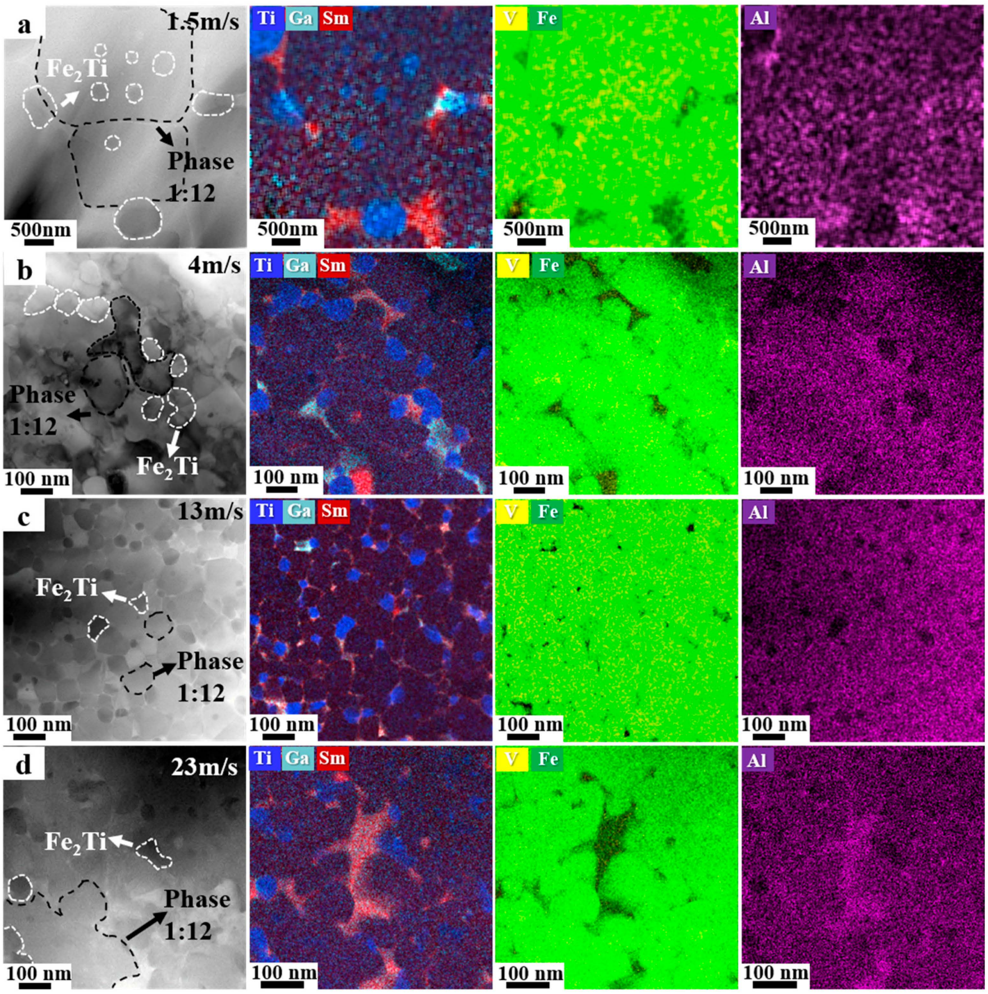

Figure 3. The HAADF image of $Sm_8Fe_{73.5}Ti_8V_8Al_2Ga_{0.5}$ alloys. (**a**) EDS mapping images of 1.5 m/s sample, (**b**) EDS mapping images of 4 m/s sample, (**c**) EDS mapping of 13 m/s sample, and (**d**) EDS mapping of 23 m/s sample.

To further investigate the microstructure of the alloy, high-resolution transmission electron microscopy (HRTEM) characterization was performed on the sample, with a cooling rate of 1.5 m/s. Figure 4 presents the TEM images and analysis results of the 1.5 m/s sample. Figure 4a shows the morphologies of 1:12 grains, Fe_2Ti grains, and Sm-rich phases. Figure 4b,c show the selected area electron diffraction (SAED) patterns of the white dashed region in Figure 4a. Figure 4d,e display high-resolution images of the red and blue boxed regions in Figure 4a. The SAED pattern is indexed in Figure 4b and was calibrated and identified as Fe_2Ti, with a zone axis of [100]. The calibration of the electron diffraction pattern in Figure 4c indicates a 1:12 main phase is in that region, with a zone axis of [001]. In Figure 4d, HRTEM imaging reveals a clear separation between the grain boundary phase and the 1:12 phase. Fourier-transform analysis on the left side of the image shows diffraction rings, which confirms its amorphous nature, while on the right side, the Fourier transform indicates the main phase with a 1:12 ratio. Figure 4e also shows the amorphous grain boundary sandwiched between the main phases. The formation of this intergranular phase is significant both for improving the coercivity in the isotropic melt-spun ribbon and obtaining anisotropic magnets using a conventional liquid sintering process [36]. In Figure 4f, the white circle represents the SAED pattern, and in Figure 4g, two diffraction spots can be observed. The zone axis is identified as [111], confirming the occurrence of twinning in this 1:12 phase, which is detrimental to coercivity [37]. Point scanning at location I in the grain boundary shows a Sm-to-Fe ratio of approximately 1:3, with Fe content as high as 67.81%. An excessively high iron content within grain boundaries can enhance magnetic exchange coupling between grains [38], which leads to poor coercivity in the 1.5 m/s samples. Elemental analysis using HAADF imaging on the white dashed box region in Figure 4f provides a clear visualization of the elemental distribution in the Fe_2Ti grain. Point scanning at location II in the Fe_2Ti phase indicates the main components being Fe_2(Ti, V) in a ratio of approximately 2:1 for Ti and V, with minimal amounts of Sm, Ga, and Al. It reveals a partial substitution of Ti by V in the Fe_2Ti phase. Line scanning at the grain boundary in Figure 4f reveals fluctuations in Sm and Fe elements, with a significant decrease in Fe and enrichment of Sm at the grain boundary. This result is very important for constructing weak magnetic grain boundary phases [13].

Subsequently, we captured Lorentz mode TEM (LTEM) images of the 1.5 m/s rapid solidification samples, and the specimens were further processed using the transport of intensity equation (TIE) method, as illustrated in Figure 5. The TIE treatment area is the red box area in Figure 5b, containing 1:12 grains, Fe_2Ti grains, and a segment of the grain boundary phase. In the TIE images, colors and arrows represent the magnitude and direction of magnetization, respectively. Figure 5c reveals an absence of magnetic domains in the Fe_2Ti region due to its paramagnetic nature at room temperature. Magnetic domains in different 1:12 grains exhibit opposing directions on either side of the grain boundaries, demonstrating the effective magnetic isolation facilitated by the non-crystalline-rich Sm, Al, and Ga grain boundaries among the 1:12 main phases. However, the appearance of Fe_2Ti grain within the main phase acts as a pinning site, introducing some demagnetizing fields and becoming centers for reverse magnetization nucleation [9]. It is necessary to regulate its distribution into the grain boundary phase to enhance the magnetic isolation effect between 1:12 grains, thus improving the coercivity of the alloy [12,39].

To explore the microstructure of the sample with the highest coercivity, TEM characterization of the 13 m/s cooling rate sample was performed, as shown in Figure 6. In Figure 6a, the sizes of the 1:12 phase and Fe_2Ti phase are of nanometer size, with clear grain boundaries between grains. Figure 6b shows an HRETM image of the marked grain in the red region of Figure 6a. The SAED pattern for the grain in region b confirms it is a $SmFe_{12}$ grain with the [111] zone axis. Point scanning at location I on the grain boundary shows a Sm-to-Fe ratio of approximately 7:9, with Fe content of 45.56%, which is lower than the 1.5 m/s sample. Reducing the Fe content in the grain boundary can result in lower magnetization, consequently weakening the intergranular exchange coupling and enhancing coercivity [8,9,40]. In Figure 6e, the SAED pattern for the grain in region d identifies it as an Fe_2Ti grain with the [100] zone axis. In the Fe_2Ti grain, the point scan reveals region II is primarily composed of Fe_2(Ti, V) with a Ti-to-V ratio of 2:1, with minimal concentrations of Sm, Ga, and Al, which is similar to the 1.5 m/s sample. In Figure 6f, the grain boundary phase appears predominantly amorphous with small $SmFe_2$ crystalline grains. This is further supported by the SAED pattern in Figure 6g, confirming that region f is composed of an amorphous and partially crystallized $SmFe_2$ phase. The HAADF image provides insights into the elemental distribution within the observed region. Sm, Ga, and Al are evenly distributed around the 1:12 grain, while Ti is mainly located at the triple junction. Compared with the 1.5 m/s sample, the distribution of Sm, Ga, and Al elements is more continuous, and most of Ti in the 1:12 grain disappears. The distribution of Fe and V elements is similar, mainly present in the 1:12 main phase and Fe_2Ti phase, with minimal presence at the grain boundaries. A blue line scan in the HAADF image also reveals fluctuations in the elemental content at the grain boundary. A decrease in Fe and V concentrations and an enrichment of Sm, Ga, and Al elements at the grain boundary are observed, while Ti shows minimal fluctuations. This result suggests that Ti exists in the form of Fe_2Ti. In summary, the TEM data provide detailed insights into the microstructure and elemental distribution of the 13 m/s sample. The grain boundary phase composed of the paramagnetic phase Fe_2Ti and the non-magnetic elements Sm, Ga, and Al helped to weaken the magnetic exchange coupling between the 1:12 grains, thus enhancing the magnetic isolation ability of the grain boundaries, which is an important factor in enhancing its coercivity.

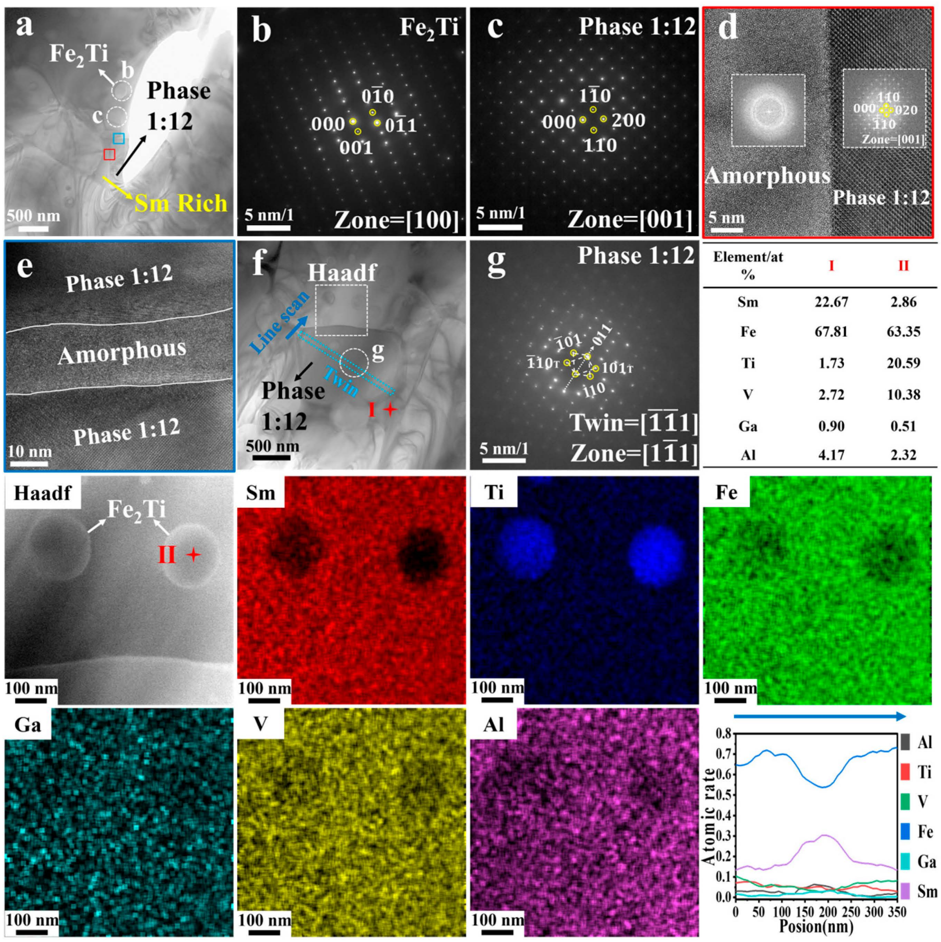

Figure 4. (**a**,**f**) TEM observation of $SmFe_{12}$ and Fe_2Ti grains in 1.5 m/s alloy; (**b**) SAED patterns of Fe_2Ti phase; (**c**) SAED patterns of 1:12 phase; (**d**) HRTEM image for the red square region in panel (**a**); (**e**) HRTEM image for the blue square region in panel (**a**); (**g**) SAED patterns for the green circle region in panel (**f**); HAADF image and corresponding EDS mapping results of different elements.

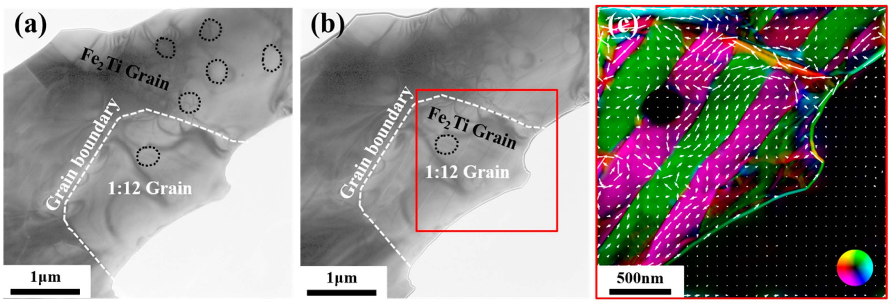

Figure 5. Spontaneous magnetic domain structure in 1.5 m/s cast alloy. (**a**) In-focused, (**b**) under-focused LTEM images, and (**c**) magnetic domain structure images obtained by TIE processing.

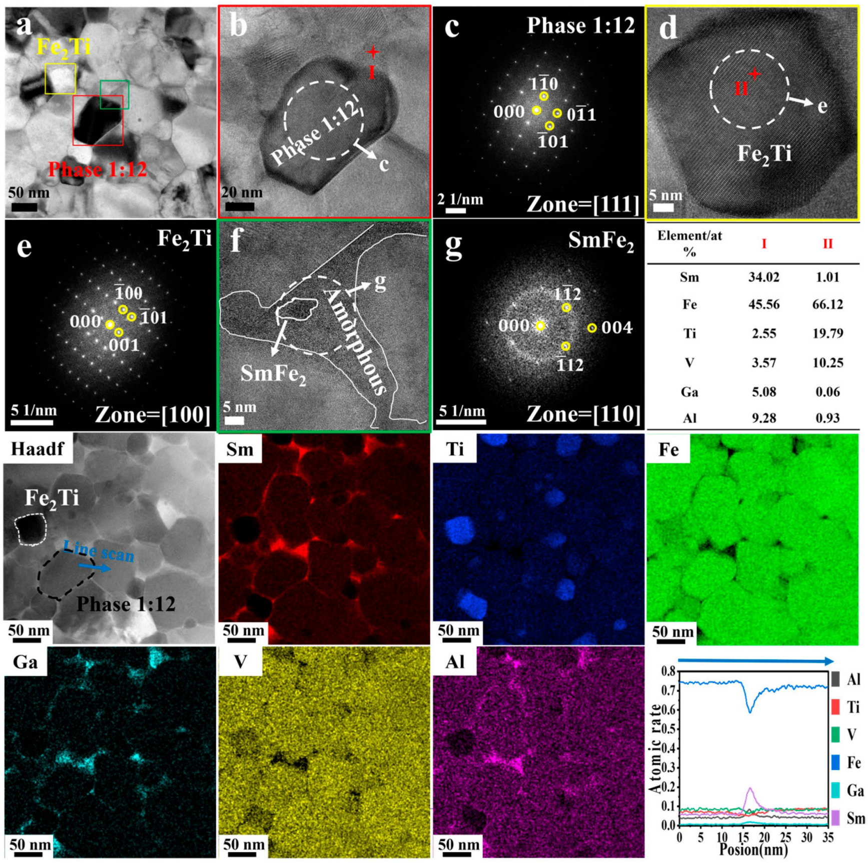

Figure 6. (**a**) TEM observation of $SmFe_{12}$ and Fe_2Ti grains in 13 m/s cast alloy; (**b**) HRTEM image for the red square region in (**a**); (**c**) SAED patterns of 1:12 phase; (**d**) HRTEM image for the yellow square region in (**a**); (**e**) SAED patterns of Fe_2Ti phase; (**f**) HRTEM image for the green square region in (**a**); (**g**) SAED patterns of triple junctions in (**f**); HAADF image and corresponding EDS mapping results of different elements.

3.3. First-Principles Calculations

First-principles calculations were conducted to investigate the effect of V elements on the magnetism of Fe_2Ti at 0 K, elucidating the magnetic properties of the Fe_2Ti ground state. Figure 7a shows the representative structure Fe_2(Ti, V), in which the element V replaces the element Ti. The formation energies of the atom substitution with different contents of V were calculated, as shown in Figure 7b. With an increase in the V substitution, the formation energy of Fe_2Ti increases. The Ti:V = 2:1 phenomenon combined with the experiment shows that the Fe_2(Ti, V) structure with a low concentration of the V element is more easily formed. The magnetic energy data are calculated based on the ferromagnetic ground state of Fe_2Ti, and the anisotropic (K_u) is very low, which proves that V has little influence on it. The detailed data can be seen in Table S1. Figure 7c shows the magnetic moments for different amounts of V substitutions. The DFT results suggest that the saturation magnetization of Fe_2Ti decreases with the increase in the V substitution, which is beneficial for its magnetic isolation ability. To investigate the effect of V substitution on the magnetic transition temperature of Fe_2Ti, the magnetic exchange coupling between Fe atoms in Fe_2Ti and $Fe_2(Ti_{0.5}V_{0.5})$ was calculated, as shown in Figure 7d. The magnetic exchange coupling between nearest-neighbor Fe and Fe atoms decreases after a V substitution. The J of Fe_2Ti is below 26 meV, indicating a relatively low magnetic ordering temperature. Furthermore, the substitution of V further reduces the magnetic ordering temperature of the Fe_2Ti phase, facilitating paramagnetic formation at room temperature and enhancing the magnetic isolation effect. To verify the findings of the calculation, we prepared Fe_2Ti using argon arc melting and tested its M-T curve, as shown in Figure S6. Two transition temperature points appeared at T_{c1} = 267 K and T_{c2} = 290 K. T_{c1} represents the magnetic transition point where the coexistence of ferromagnetic and antiferromagnetic phases within Fe_2Ti changed into the antiferromagnetic phase, [41,42], while T_{c2} denotes its Neel temperature point, indicating the paramagnetic behavior of Fe_2Ti at room temperature [25].

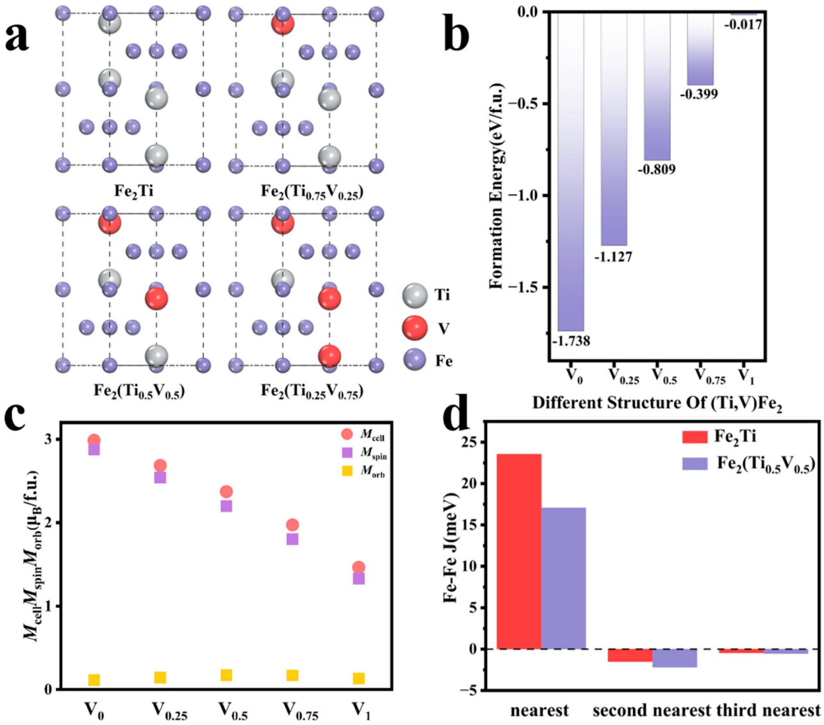

Figure 7. (**a**) Crystal structures of $Fe_2(Ti_{1-x}V_x)$, x = 0~0.75; (**b**) formation energies of $Fe_2(Ti_{1-x}V_x)$, x = 0~1; (**c**) total magnetic moment M_{cell}, spin magnetic moment M_{spin} and orbital magnetic moment M_{orb} of $Fe_2(Ti_{1-x}V_x)$, x = 0~1; (**d**) magnetic exchange coupling between Fe and Fe in Fe_2Ti and $Fe_2(Ti_{0.5}V_{0.5})$.

3.4. Magnetic Simulation

Based on the optimization of the alloy's microstructure observed in TEM images, we proposed schematic micromagnetic models to explain the mechanism of coercivity enhancement. It represents three scenarios: Figure 8a where the grain boundary phase does not contain Fe_2Ti, Figure 8b where the grain boundary phase contains Fe_2Ti, and Figure 8c where Fe_2Ti is distributed between the grain boundary phase and the grains of the 1:12 main phase. Based on these experimental phenomena, we constructed three models, as shown in Figure 8d–f. In the models, the blue area represents 1:12 grains, the cyan area represents Fe_2Ti grains, the gray area represents the Sm-rich grain boundary phase, and the yellow arrows point to the Fe_2Ti grains. Figure 8g–i depict the demagnetization process of models 1–3 under an external magnetic field. The initial red region represents the demagnetized area (parallel to the positive Z-axis), while the blue region indicates the nucleation area of demagnetization. As shown in Figure 8g, demagnetization domains form at lower external magnetic fields and nucleate rapidly between grains [43], with a coercive force of H_c = 52.52 kOe in model 1. As shown in Figure 8h, due to the magnetic isolation effect provided by the presence of the Fe_2Ti secondary phase between adjacent 1:12 phase grains [16], the coercivity of the magnet increases to 56.55 kOe in model 2. As shown in Figure 8i, although the Fe_2Ti in the grain boundaries can hinder the propagation of demagnetization domains, Fe_2Ti particles within the grains still cannot effectively prevent the magnetization reversal of the entire grain, so the coercivity of the magnet decreases to 55.29 kOe in model 3. According to the comprehensive micromagnetic simulation results, Fe_2Ti in the grain boundaries exhibits an effective pinning effect against the propagation of the demagnetization domain wall, leading to higher coercivity. The demagnetization curves of models 1–3 are shown in Figure 8j, where the coercive force of model 2 is significantly enhanced accompanied by a decrease in residual magnetism due to the enhanced magnetic isolation between adjacent grains. Additionally, the presence of Fe_2Ti within the main phase in model 3 reduces the effectiveness of grain isolation, resulting in a lower increase in coercivity and a decrease in residual magnetism.

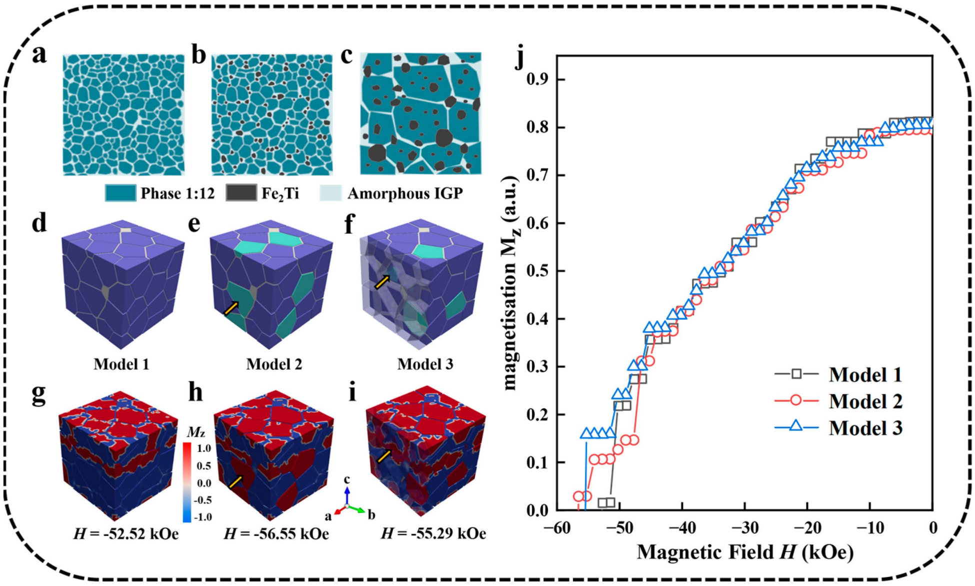

Figure 8. (**a**) Schematic diagram of continuous Sm-rich grain boundary phase encapsulation 1:12 main phase; (**b**) schematic diagram of continuous Sm-rich grain boundary combined with Fe2Ti phase encapsulation 1:12 main phase; (**c**) schematic diagram of random distribution of Fe_2Ti; (**d**,**e**) the micromagnetic simulation model corresponding to the schematic diagram; (**g**–**i**) demagnetization process of models (**d**–**f**); (**j**) simulated demagnetization curves.

4. Conclusions

We constructed a weak magnetic grain boundary phase containing Fe_2Ti in $SmFe_{12}$-based alloys by controlling the cooling speed. The magnetic isolation effect of Fe_2Ti successfully increased the coercivity of the alloy from 3.13 kOe to 7.95 kOe, as demonstrated by LTEM and further confirmed by micromagnetic simulations. TEM confirms that the distribution of Fe_2Ti in the alloy can be regulated by a proper cooling rate. Moreover, first-principles calculations reveal that the doping of V elements facilitates the paramagnetic formation of Fe_2Ti at room temperature. The increase in coercivity in this work (4.82 kOe) is higher than that in similar work by Liu [16] (3 kOe). This work provides a new method for regulating the distribution of the Fe_2Ti grain boundary phase in $SmFe_{12}$-based magnets by adjusting the cooling rate while maintaining the stability of the $SmFe_{12}$ phase, to construct a continuous non-magnetic grain boundary phase. This finding can promote the industrialization of high-coercivity $SmFe_{12}$-based magnets, thereby advancing technology in electric motors.

Supplementary Materials: The following supporting information can be downloaded at: https://www.mdpi.com/article/10.3390/cryst14060572/s1, Figure S1. Demagnetization curve of the $Sm_8Fe_{73.5}Ti_8V_8Al_2Ga_{0.5}$ alloys with different cooling rates varying from 1.5 m/s to 33 m/s. Figure S2. Demagnetization curve (a) and enlarged view of the demagnetization curves (b) of the $Sm_8Fe_{73.5}Ti_8V_8Al_2Ga_{0.5}$ alloys with different cooling rates varying from 1.5 m/s to 8 m/s. Figure S3. (a,f) TEM observation of $SmFe_{12}$, α-Fe, and Fe_2Ti grains in 4 m/s alloy; (b) HRTEM image for the red square region in Figure S3a; (c) SAED patterns of 1:12 phase; (d) HRTEM image for the green square region in Figure S3a; (e) SAED patterns of Fe_2Ti phase; (g) HRTEM image for the yellow square region in Figure S3f; (h) SAED patterns of α-Fe phase. Figure S4. (a) TEM observation of $SmFe_{12}$ and Fe_2Ti grains in 23 m/s cast alloy; (b) HRTEM image for the yellow square region in Figure S4a; (c) SAED patterns of grain boundary; (d) HRTEM image for the red square region in Figure S4b; (e) SAED patterns of 1:12 phase; (f) HRTEM image for the green square region in Figure S4b; (g) SAED patterns of Fe_2Ti phase; Point scan data at different locations. Figure S5. The HAADF image of $Sm_8Fe_{73.5}Ti_8V_8Al_2Ga_{0.5}$ alloys. (a) EDS mapping images of 1.5 m/s sample, (b) EDS mapping images of 4 m/s sample, (c) EDS mapping of 13 m/s sample, and (d) EDS mapping of 23 m/s sample. Figure S6. MT curve of Fe_2Ti. Table S1. Magnetic properties of the $Sm_8Fe_{73.5}Ti_8V_8Al_2Ga_{0.5}$ alloys with different cooling rates varying from 1.5 m/s to 8 m/s. Table S2. Anisotropy value K_u of $Fe_2(Ti_{1-x}V_x)$, x = 0~1. Table S3. Comparison of coercivity data with similar work.

Author Contributions: Conceptualization, J.W.; methodology J.W., X.L. and L.Z.; data curation, J.W., S.X. and C.X.; investigation, J.W.; software, S.X., C.X. and Y.P.; writing—original draft preparation, J.W. and L.Z.; writing—review and editing, J.W., Y.P. and L.Z.; supervision, Y.P., L.Z. and X.Z.; funding acquisition, L.Z., W.W., Y.W., P.C., J.L. and X.Z.; validation, W.W., Y.W., P.C., J.L., L.Z. and X.Z. All authors have read and agreed to the published version of the manuscript.

Funding: This work was supported by the National Science Fund for Distinguished Young Scholars (No. 52225312), National Natural Science Foundation of China (No. 52171175), Key R&D Projects of Zhejiang Province (No. 2023C01077), and National Key R&D Program of China (2023YFB3507502).

Data Availability Statement: The original contributions presented in this study are included in the article/Supplementary Material; further inquiries can be directed to the corresponding authors.

Acknowledgments: We express our gratitude to Hangzhou Dianzi University and Zhejiang Magnetic Materials Research Center for supporting our work.

Conflicts of Interest: Author Wei Wang, Yue Wu, Ping Chen and Jun Liu were employed by the company Ningbo Shouzheng Magnet Co., Ltd. The remaining authors declare that the research was conducted in the absence of any commercial or financial relationships that could be construed as a potential conflict of interest.

References

1. Pathak, A.K.; Khan, M.; Gschneidner, K.A., Jr.; Mccallum, R.W.; Zhou, L.; Sun, K.; Dennis, K.W.; Zhou, C.; Pinkerton, F.E.; Kramer, M.J. Cerium: An unlikely replacement of dysprosium in high performance NdFeB permanent magnets. *Adv. Mater.* **2015**, *27*, 2663–2667. [CrossRef] [PubMed]
2. Gutfleisch, O.; Willard, M.A.; Brück, E.; Chen, C.H.; Sankar, S.G.; Liu, J.P. Magnetic materials and devices for the 21st century: Stronger, lighter, and more energy efficient. *Adv. Mater.* **2011**, *23*, 821–842. [CrossRef] [PubMed]
3. Li, X.; Lou, L.; Song, W.; Huang, G.; Hou, F.; Zhang, Q.; Zhang, H.T.; Xiao, J.; Wen, B.; Zhang, X. Novel bimorphological anisotropic bulk nanocomposite materials with high energy products. *Adv. Mater.* **2017**, *29*, 1606430. [CrossRef] [PubMed]
4. Zhao, L.; He, J.; Li, W.; Liu, X.; Zhang, J.; Wen, L.; Zhang, Z.; Hu, J.; Zhang, J.; Liao, X. Understanding the role of element grain boundary diffusion mechanism in Nd–Fe–B magnets. *Adv. Funct. Mater.* **2022**, *32*, 2109529. [CrossRef]
5. Sepehri-Amin, H.; Tamazawa, Y.; Kambayashi, M.; Saito, G.; Takahashi, Y.K.; Ogawa, D.; Ohkubo, T.; Hirosawa, S.; Doi, M.; Shima, T. Achievement of high coercivity in Sm $(Fe_{0.8}Co_{0.2})_{12}$ anisotropic magnetic thin film by boron doping. *Acta Mater.* **2020**, *194*, 337–342. [CrossRef]
6. Hirayama, Y.; Takahashi, Y.K.; Hirosawa, S.; Hono, K. Intrinsic hard magnetic properties of Sm $(Fe_{1-x}Co_x)_{12}$ compound with the $ThMn_{12}$ structure. *Scr. Mater.* **2017**, *138*, 62–65. [CrossRef]
7. Sakuma, A.; Tanigawa, S.; Tokunaga, M. Micromagnetic studies of inhomogeneous nucleation in hard magnets. *J. Magn. Magn. Mater.* **1990**, *84*, 52–58. [CrossRef]

8. Otsuka, K.; Kamata, M.; Nomura, T.; Iida, H.; Nakamura, H. Coercivities of Sm–Fe–M sintered magnets with $ThMn_{12}$-type structure (M = Ti, V). *Mater. Trans.* **2021**, *62*, 887–891. [CrossRef]
9. Zhang, J.S.; Tang, X.; Sepehri-Amin, H.; Srinithi, A.K.; Ohkubo, T.; Hono, K. Origin of coercivity in an anisotropic Sm (Fe, Ti, V) $_{12}$-based sintered magnet. *Acta Mater.* **2021**, *217*, 117161. [CrossRef]
10. Tang, X.; Li, J.; Srinithi, A.K.; Sepehri-Amin, H.; Ohkubo, T.; Hono, K. Role of V on the coercivity of SmFe12-based melt-spun ribbons revealed by machine learning and microstructure characterizations. *Scr. Mater.* **2021**, *200*, 113925. [CrossRef]
11. Samata, H.; Fujiwara, N.; Nagata, Y.; Uchida, T.; Der Lan, M. Magnetic anisotropy and magnetostriction of $SmFe_2$ crystal. *J. Magn. Magn. Mater.* **1999**, *195*, 376–383. [CrossRef]
12. Tozman, P.; Sepehri-Amin, H.; Hono, K. Prospects for the development of SmFe12-based permanent magnets with a $ThMn_{12}$-type phase. *Scr. Mater.* **2021**, *194*, 113686. [CrossRef]
13. Srinithi, A.K.; Tang, X.; Sepehri-Amin, H.; Zhang, J.; Ohkubo, T.; Hono, K. High-coercivity $SmFe_{12}$-based anisotropic sintered magnets by Cu addition. *Acta Mater.* **2023**, *256*, 119111. [CrossRef]
14. Zhang, J.S.; Tang, X.; Bolyachkin, A.; Srinithi, A.K.; Ohkubo, T.; Sepehri-Amin, H.; Hono, K. Microstructure and extrinsic magnetic properties of anisotropic Sm $(Fe, Ti, V)_{12}$-based sintered magnets. *Acta Mater.* **2022**, *238*, 118228. [CrossRef]
15. Martins, T.B.; Rechenberg, H.R. Antiferromagnetic $TiFe_2$ in applied fields: Experiment and simulation. *Hyperfine Interact.* **2006**, *169*, 1273–1277. [CrossRef]
16. Liu, Z.; Liu, Z.; Wu, H.; Zhu, C.; Cheng, W.; Cao, S.; Luo, H.; Wu, L.; Chen, R.; Xia, W. Mechanism of Ti-rich grain boundary phase formation and coercivity reinforcement in Sm $(Fe_{0.8}Co_{0.2})_{11}TiB_x$ melt-spun ribbons. *Scr. Mater.* **2023**, *227*, 115281. [CrossRef]
17. Dirba, I.; Harashima, Y.; Sepehri-Amin, H.; Ohkubo, T.; Miyake, T.; Hirosawa, S.; Hono, K. Thermal decomposition of $ThMn_{12}$-type phase and its optimum stabilizing elements in $SmFe_{12}$-based alloys. *J. Alloys Compd.* **2020**, *813*, 152224. [CrossRef]
18. Toby, B.H.; Von Dreele, R.B. GSAS-II: The genesis of a modern open-source all purpose crystallography software package. *J. Appl. Crystallogr.* **2013**, *46*, 544–549. [CrossRef]
19. Zhao, L.; Li, C.; Zhang, X.; Bandaru, S.; Su, K.; Liu, X.; Zhou, Q.; Li, L.; Grenrche, J.; Jin, J. Effects of Sm content on the phase structure, microstructure and magnetic properties of the SmxZr0. 2 (Fe0.8Co0.2) 11.5 Ti0. 5 (x = 0.8–1.4) alloys. *J. Alloys Compd.* **2020**, *828*, 154428. [CrossRef]
20. Zhao, L.; Grenrche, L. On the magnetism of grain boundary phase and its contribution to the abnormal openness of recoil loops in hot-deformed magnets. *J. Phys. D Appl. Phys.* **2020**, *53*, 095002. [CrossRef]
21. Scholz, W.; Fidler, J.; Schrefl, T.; Suess, D.; Forster, H.; Tsiantos, V. Scalable parallel micromagnetic solvers for magnetic nanostructures. *Comput. Mater. Sci.* **2003**, *28*, 366–383. [CrossRef]
22. Duy, T.V.T.; Ozaki, T. A three-dimensional domain decomposition method for large-scale DFT electronic structure calculations. *Comput. Phys. Commun.* **2014**, *185*, 777–789. [CrossRef]
23. Ozaki, T.; Kino, H. Efficient projector expansion for the ab initio LCAO method. *Phys. Rev. B* **2005**, *72*, 45121. [CrossRef]
24. Ozaki, T.; Kino, H. Numerical atomic basis orbitals from H to Kr. *Phys. Rev. B* **2004**, *69*, 195113. [CrossRef]
25. Ozaki, T. Variationally optimized atomic orbitals for large-scale electronic structures. *Phys. Rev. B* **2003**, *67*, 155108. [CrossRef]
26. Matsumoto, M.; Hawai, T.; Ono, K. (Sm, Zr)$Fe_{12-x}M_x$ (M = Zr, Ti, Co) for permanent-magnet applications: Ab initio material design integrated with experimental characterization. *Phys. Rev. Appl.* **2020**, *13*, 64028. [CrossRef]
27. Perdew, J.P.; Burke, K.; Ernzerhof, M. Generalized gradient approximation made simple. *Phys. Rev. Lett.* **1996**, *77*, 3865. [CrossRef]
28. Terasawa, A.; Matsumoto, M.; Ozaki, T.; Gohda, Y. Efficient algorithm based on liechtenstein method for computing exchange coupling constants using localized basis set. *J. Phys. Soc. Jpn.* **2019**, *88*, 114706. [CrossRef]
29. Han, M.J.; Ozaki, T.; Yu, J. Electronic structure, magnetic interactions, and the role of ligands in Mn_n (n=4,12) single-molecule magnets. *Phys. Rev. B* **2004**, *70*, 184421. [CrossRef]
30. Liechtenstein, A.I.; Katsnelson, M.I.; Antropov, V.P.; Gubanov, V.A. Local spin density functional approach to the theory of exchange interactions in ferromagnetic metals and alloys. *J. Magn. Magn. Mater.* **1987**, *67*, 65–74. [CrossRef]
31. Wu, C.; Lin, K.J.; Cheng, Y.T.; Huang, C.; Pan, C.N.; Li, W.C.; Chiang, L.; Yeh, C.; Fong, S. Development of amorphous ribbon manufacturing technology. *China Steel Tech. Rep.* **2014**, *27*, 28–42.
32. Liebermann, H.H. Rapidly solidified alloys made by chill block melt-spinning processes. *J. Cryst. Growth* **1984**, *70*, 497–506. [CrossRef]
33. Fitzpatrick, J.R.; Ellis, B. X-ray diffraction studies of the structure of amorphous polymers. In *The Physics of Glassy Polymers*; Springer: Berlin/Heidelberg, Germany, 1973; pp. 108–152. [CrossRef]
34. Tamura, T.; Li, M. Influencing factors on the amorphous phase formation in Fe–7.7 at% Sm alloys solidified by high-speed melt spinning. *J. Alloys Compd.* **2020**, *826*, 154010. [CrossRef]
35. Demirel, A.; Çetin, E.C.; Karakuş, A.; Ataş, M.Ş.; Yildirim, M. Microstructural Evolution and oxidation BEhavior of fe-4cr-6ti fErritic alloy with fe2ti lavEs PhasE PrEciPitatEs. *Arch. Metall. Mater.* **2022**, *67*, 827–836. [CrossRef]
36. Hono, K.; Sepehri-Amin, H. Reprint of Prospect for HRE-free high coercivity Nd-Fe-B permanent magnets. *Scr. Mater.* **2018**, *154*, 277–283. [CrossRef]
37. Ener, S.; Skokov, K.P.; Palanisamy, D.; Devillers, T.; Fischbacher, J.; Eslava, G.G.; Maccari, F.; Schäfer, L.; Diop, L.V.; Radulov, I. Twins–A weak link in the magnetic hardening of ThMn12-type permanent magnets. *Acta Mater.* **2021**, *214*, 116968. [CrossRef]

38. Palanisamy, D.; Ener, S.; Maccari, F.; Schäfer, L.; Skokov, K.P.; Gutfleisch, O.; Raabe, D.; Gault, B. Grain boundary segregation, phase formation, and their influence on the coercivity of rapidly solidified $SmFe_{11}Ti$ hard magnetic alloys. *Phys. Rev. Mater.* **2020**, *4*, 54404. [CrossRef]
39. Koeble, J.; Huth, M. Field induced unidirectional magnetic anisotropy in Fe_2Ti thin films. In *Materials Science Forum*; Trans Tech Publications Ltd.: Zurich-Uetikon, Switzerland, 2001; pp. 137–140. [CrossRef]
40. Hono, K.; Sepehri-Amin, H. Strategy for high-coercivity Nd–Fe–B magnets. *Scr. Mater.* **2012**, *67*, 530–535. [CrossRef]
41. Wu, Y.; Wu, X.; Qin, S.; Yang, K. Compressibility and phase transition of intermetallic compound Fe_2Ti. *J. Alloys Compd.* **2013**, *558*, 160–163. [CrossRef]
42. Pelloth, J.; Brand, R.A.; Keune, W. Local magnetic properties of the Fe_2Ti Laves phase. *J. Magn. Magn. Mater.* **1995**, *140*, 59–60. [CrossRef]
43. Li, J.; Tang, X.; Sepehri-Amin, H.; Sasaki, T.T.; Ohkubo, T.; Hono, K. Angular dependence and thermal stability of coercivity of Nd-rich Ga-doped Nd–Fe–B sintered magnet. *Acta Mater.* **2020**, *187*, 66–72. [CrossRef]